UC Riverside
Other Recent Work

Title

Characterizing GNSS Multipath at Different Antenna Mounting Positions on Vehicles

Permalink

https://escholarship.org/uc/item/9mj3459s

Authors

Uwineza, Jean-Bernard
Rahman, Farzana
Silva, Felipe
et al.

Publication Date

2019-12-17

Data Availability

The data associated with this publication are available upon request.

Characterizing GNSS Multipath at Different Antenna Mounting Positions on Vehicles

Jean-Bernard Uwineza, Farzana Rahman, Felipe Silva, Wang Hu, Jay A. Farrell

Department of Electrical and Computer Engineering, University of California, Riverside, CA 92521

I. EXECUTIVE SUMMARY

This document presents an analysis of antenna performance as a function of installation position on a vehicle. Each of three antennas is evaluated at three different installation locations on top of a car: front, middle, and rear along the car center-line (see Fig. 2).

The equipment and experimental procedures are described in Section II. GPS measurement models are reviewed in Section III. Performance is analyzed by two methods. The first analysis approach uses differential GPS (DGPS) estimated position relative to a ground truth antenna position. The second analysis approach directly analyzes the statistics of the estimated multipath signal for each satellite. The methodology for each analysis approach is described in Sections IV and V. The experimental results are presented in Section VI.

The method for determining ground truth for the DGPS analysis approach is presented in Appendix A. The method for estimating Ionospheric delay for the multipath signal analysis is presented in Appendix B. Example Ionospheric delay calculations are include in Appendix C. The elevation and signal strength thresholds used to select the epochs to be included in this study are discussed in Appendix D.

The conclusions related to performance are as follows. Among the antennas, the Sharkfin consistently performed worse than the other two antennas. Between the single and multi-band patch antennas, the performance was similar with the multi-band antenna performing better by some measures (e.g. position estimation histogram and standard deviation) and the single-band antenna performing better by other measures (e.g., multi-path standard deviation). The rear antenna location yielded slightly better performance, but the differences in performance between the three mounting locations was not large and therefore somewhat inconclusive.

II. EQUIPMENT & PROCEDURES

This section describes various aspects of the experimental procedure.

A. Vehicle Antenna Placement

The experiment consists of three data collection intervals, each of approximately equal duration, starting at approximately the same time, over three consecutive days. For the entire three day period, a Nissan Altima sedan (shown in Fig. 1) was parked in the same location. On the first day of data collection, the roof of the vehicle was marked with a strip of masking tape from front to back. The tape was marked with three trial locations: near the front, middle, and back of the roof. See the illustration in Fig. 2. Because the antenna center could be accurately placed at the location marked on the tape, mounting positions are considered accurate to less than one centimeter, which is significantly less than the meter level multipath effects that are being analyzed. Therefore, mounting inaccuracy is neglected in the analysis.

This procedure – using the vehicle at the same location and taking measurements over the same time intervals – is intended to cause the multipath effects to be similar between the three data sets because multipath signals at the same location are highly correlated from one day to the next.

This allows each antenna to be evaluated at each of three mounting locations enabling comparison both between antennas and mounting locations. Each day each of the three antennas was mounted at a different location as summarized in Table I. The analysis of multipath effects via DGPS positioning analysis will compare the estimated position with a ground truth antenna location. The method to compute this ground truth antenna location is described in Appendix A

B. Receivers and Antennas

The experiment used three Ardusimple application boards with the u-blox ZED-F9P GNSS positioning module to measure the satellite signals. One receiver was connected to each antenna.

The three antennas under test are as follows:

Table I Antenna mounting locations per day.

	Front	Middle	Rear
Day 1	Patch	Sharkfin	Multiband
Day 2	Multiband	Patch	Sharkfin
Day 3	Sharkfin	Multiband	Patch

Figure 1: Vehicle and location used in the experiment.

(a) u-blox single frequency antenna (i.e., Model ANN-MS-1);
(b) u-blox multiband antenna (i.e., Model ANN-MB-01);
(c) MOPAR Sharkfin antenna (i.e., Model 40908H).

The u-blox multiband antenna allows dual-frequency measurements [1], which enables estimation and removal of Ionospheric effects. See Appendix B.

The GISA CORS station located at ESRI uses a Trimble NetR9 reference receiver, and a Trimble Zephyr Geodetic antenna (i.e. TRM55971.00_NONE). Data from this receiver was used to compute the DGPS corrections for the positioning experiments and the Ionospheric delay estimate for the multipath analysis.

C. Experiment Procedure

The experimental data was acquired on three days from October 30th to November 2nd, 2019, over the same time interval, 17:00 to 21:00 PST (00:00 to 04:00 UTC). On each day, data from each of the three antennas were collected concurrently. Each day produced three data sets, one for each antenna, resulting in nine datasets for the entire experiment.

The u-blox u-center software recorded the GNSS receiver data. Simultaneously, a separate computer also recorded real-time raw measurements from the GISA CORS base station via NTRIP for use in DGNSS positioning. The raw data from GPS, GLONASS, and Galileo constellations were recorded and utilized to get a more accurate ground-truth position for the antenna locations. The multipath analysis only used the L1 GPS measurements.

III. BACKGROUND: GPS SIGNAL MODELS

This section reviews the GPS measurement models [2]–[4].

The code and phase-range models for measurements from satellite s by receiver r (on the L1 signal) are

$$\rho_r^s = R_r^s + c(dt_r - dt^s) + I_{r,1}^s + T_r^s + M_\rho^s + K_p^s + \eta_\rho^s \quad (1)$$

$$\phi_r^s = R_r^s + c(dt_r - dt^s) - I_{r,1}^s + T_r^s + m_\phi^s - K_r^s - \lambda N_r^s + \eta_\phi \quad (2)$$

where R_r^s is the Euclidean distance from receiver to satellite antenna, dt_r and dt^s are receiver and satellite clock errors, $I_{r,1}^s$ and T_r^s represent ionospheric and tropospheric delay, M_ρ^s and m_ϕ^s are code and phase multipath errors, K_p^s and K_r^s are code and
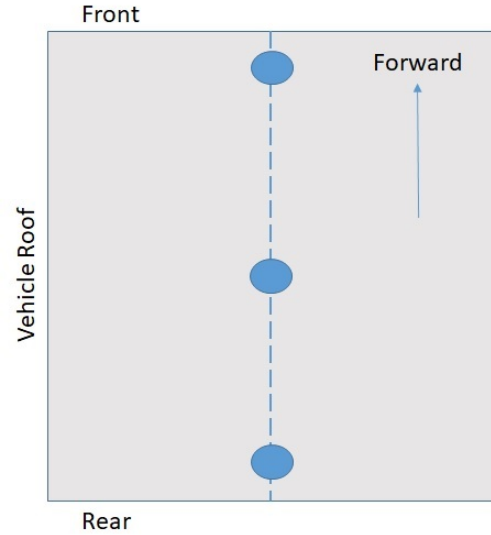

Figure 2: Antenna arrangement on car roof.

phase tracking errors induced by receiver dynamics, N_r^s is the phase ambiguity, λ is the signal wavelength, and η_ρ^s and η_ϕ^s are independent white Gaussian noise [3], [5]–[7].

Assumption 3.1: – The analysis uses these assumptions:

1) The carrier multipath error is small (i.e., ≤ 5 cm) [6]–[8].
2) The phase measurement noise is small (i.e., ≤ 1 cm) [5].
3) The receiver tracking-loop bandwidth is sufficiently high that K_p^s and K_r^s are small [5], [6].

Finally, we assume that the phase signal has been corrected for cycle slips so that N_r^s is a constant. △

Because these error terms in Assumption 3.1 are small relative to the meter level size expected for multipath, they will be ignored in the subsequent analysis. Also, this model does not include the constant hardware biases of the receiver or satellite. Such constants are discussed in relation to eqn. (13) in Section V. See also the more detailed discussion of Appendix B.

IV. DGPS POSITION ESTIMATION APPROACH

The differential correction at time t is computed from the CORS station data as

$$\tilde{c}^s(t) = \rho_b^s(t) - R(p_b, \hat{p}^s(t)) - c\hat{t}_b(t) + c\hat{t}^s(t) \quad (3)$$

where ρ_b^s is the base pseudorange measurement, p_b is the known base station location, $\hat{p}^s$ is the satellite position computed from the broadcast ephemeris, $\hat{t}^s$ is the satellite clock error computed from the broadcast ephemeris, $R(p_b, \hat{p}^s(t)) = \|p_b - \hat{p}^s\|$ is the computed base-satellite range, and $c\hat{t}_b$ is an estimate of the base receiver clock bias. Based on the pseudorange measurement model in eqn. (1), the model for $\tilde{c}^s(t)$ is

$$\tilde{c}^s(t) \doteq I_{b,1}^s(t) + T_b^s(t) + E^s(t) - c\delta t^s(t) + M_b^s(t) + \eta_b^s(t) \quad (4)$$

where $E^s = R(p_b, p^s) - R(p_b, \hat{p}^s)$ is the satellite ephemeris error and $c\delta t^s = ct^s - c\hat{t}^s$ is the residual satellite clock bias. The terms
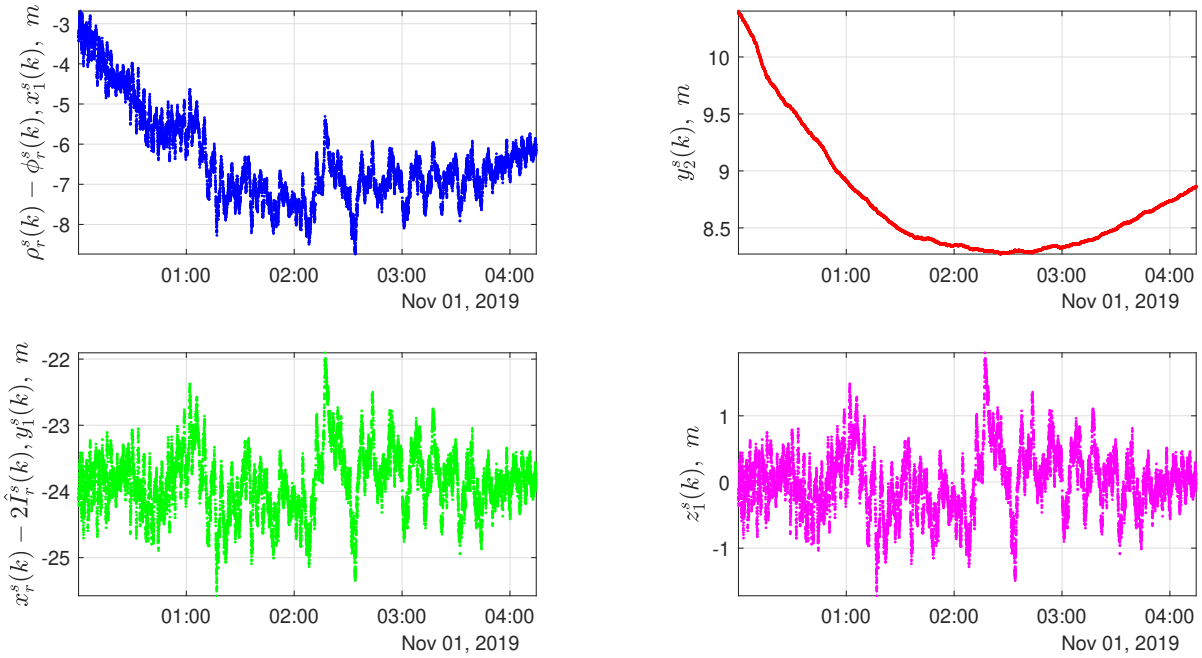
Figure 3: Example signals for estimating the L1 code multipath signal affecting *PRN* 9. See Section V.

$I_{b,1}^s(t) + T_b^s(t) + E^s(t) - c\delta t^s(t)$ represent the desired common-mode errors that should be in the DGPS correction. The remaining terms $M_b^s(t) + \eta_b^s(t)$ are unique to each receiver.

The DGPS correction computed by eqn. (3) is subtracted from each receiver pseudorange measurement prior to use in the position estimation algorithm. The linearised measurement model is:

$$\mathbf{z}_k \doteq \mathbf{H}\,x_k + \eta_k. \tag{5}$$

The rover state vector is

$$\boldsymbol{x}_k = [\mathbf{p}_r^\top(k), t_r(k)] \in \mathbb{R}^4 \tag{6}$$

where $\mathbf{p}_r \in \mathbb{R}^3$ is the rover position and $t_r \in \mathbb{R}$ is its clock bias. The observation matrix $\mathbf{H}$ is

$$\mathbf{H} = \begin{bmatrix} \hat{\mathbf{h}}_m & \mathbf{1}_m \end{bmatrix} \tag{7}$$

where m is the number of satellites, and $\hat{\mathbf{h}}_m = [\mathbf{h}^1,\ \mathbf{h}^2,\ \cdots,\ \mathbf{h}^m]^\top$ with each line-of-sight vector $\mathbf{h}^s$ calculated as

$$\mathbf{h}^s = \frac{\mathbf{p}_r - \mathbf{p}^s}{|\mathbf{p}_r - \mathbf{p}^s|} \tag{8}$$

evaluated at the prior estimate.

Results are presented for state estimation both by least-squares and Kalman filter estimation methods [3]. The Kalman filter results are computed using RTKLIB with its stationary time transition model [9].

V. Multipath Estimation Approach

This section uses the available code and phase measurements to derive a multipath signal estimate. An example signal is the pink curve in Fig. 3.

1) Given measurements of $\rho_r^s(k)$ and $\phi_r^s(k)$ at time t_k, define the signal

$$x_1^s(k) = \rho_r^s(k) - \phi_r^s(k). \tag{9}$$

Differencing eqns. (1) and (2), the model for $x_1^s(k)$ is:

$$x_1^s(k) \doteq 2I_{r,1}^s(k) + M_p^s(k) + \lambda N_r^s + \eta_{x_1}^s(k) \tag{10}$$

where the difference operation removes the range, clock terms, and tropospheric error. The symbol $\eta_{x_1}^s(k)$ accounts predominantly for pseudorange measurement error, plus the residual errors related to Assumption 3.1. The hardware biases are ignored, as these will be removed in Step 3 below.

2) If an estimate $\hat{I}_r^s(k)$ of the ionospheric error is available (See Appendix B), it can be subtracted to generate the new signal

$$y_1^s(k) = x_r^s(k) - 2\hat{I}_r^s(k) \tag{11}$$

which has the model

$$y_1^s(k) \doteq M_p^s(k) + \lambda N_r^s + \eta_{y_1}^s(k). \tag{12}$$

The symbol $\eta_{y_1}^s(k)$ adds the residual ionospheric error $2(I_{r,1}^s(k) - \hat{I}_{r,1}^s(k))$ to $\eta_{x_1}^s(k)$. This residual ionospheric error is much smaller and more slowly time-varying than the code multipath M_p^s. The signal $y_1^s(k)$ contains the multipath, plus

constant and very slowly varying terms that will be removed in the next step.

3) Because cycle slips have been corrected, N_r^s is a constant. Denote the time average of $y_1^s(k)$ as $\bar{y}_1^s$, which will include λN_r^s plus receiver and satellite hardware biases not accounted for in the above analysis. The final multipath estimate signal is computed as

$$z_1^s(k) = y_r^s(k) - \bar{y}_1^s, \tag{13}$$

which has the model

$$z_1^s(k) = M_P^s(k) + \eta_{z_1}^s(k). \tag{14}$$

The signal $z_1^s(k)$ will be analyzed for each antenna in each location to characterize multipath. The symbol $\eta_{z_1}^s(k)$ includes pseudorange measurement noise and the various residual errors neglected during the analysis.

Fig. 3 shows an example of multipath signal extraction by the method described in this section. The blue curve in the upper left is the signal $x_1^s(k)$ defined in eqn. (9) by differencing the L1 code and phase, with both expressed in units of meters. The error model of eqn. (10) shows that this should be the sum of ionospheric delay, multipath, noise, and a constant error. The ionospheric delay estimate is shown as the red curve in the upper right. Subtracting twice the ionospheric delay from $x_1^s(k)$ yields $y_1^s(k)$ as defined in eqn. (11). This signal is shown as the green curve in the bottom left. Eqn. (12) shows that this should be multipath, plus noise, plus a constant bias. Removing the mean of the signal eliminates the constant bias to yield the signal $z_1^s(k)$ as defined by eqn. (14). The signal $z_1^s(k)$ is shown as the pink curve on the bottom right.

VI. Experimental Results

This section presents the results of multipath assessment using two methods: DGPS horizontal position error and multipath signals analysis.

During data acquisition, satellite elevation and signal strength vary with time. The results in this section exclude data for which the elevation is less than 15 degrees or the signal strength is less than 30 dB. Additional discussion of the role of elevation and signal strength thresholds is presented in Appendix D.

A. DGPS Horizontal Positioning Results

At each epoch, each antenna position was estimated using DGPS corrections computed for the GISA CORS base station located in Redlands, CA (about 13 km from the test site). Since both the base station and rover data were collected simultaneously in real-time, there is negligible correction latency.

The accuracy metric used is the norm of the horizontal position error defined as

$$e_k^{al} = \left\| \begin{bmatrix} 1 & 0 & 0 \\ 0 & 1 & 0 \end{bmatrix} (\hat{\mathbf{p}}_k^a - \mathbf{p}_l) \right\| \tag{15}$$

where $\hat{\mathbf{p}}_k^a$ is the estimated antenna position for antenna a at time k, and $\mathbf{p}_l$ is the known ground truth position for location l. Both

position vectors are expressed in the North-East-Down navigation frame.

For each antenna in each of the three test locations, Fig. 4 presents the mean, standard deviation, and the entire histogram of the horizontal position error relative to ground truth. The method of computing the ground truth position is discussed in Appendix A. The upper nine graphs labeled Fig. 4a correspond to position estimation via least squares. The lower nine graphs labeled Fig. 4b correspond to position estimation via an Extended Kalman Filter (EKF) as implemented in RTKLIB.

In this analysis, all position estimation results only used single frequency pseudorange estimates and the same differential corrections. Therefore, the multifrequency capabilities of Antenna b were not needed or utilized due to the differential approach. The multifrequency measurements would be a significant benefit if non-differential operations for removal of ionospheric effects [10], [11]. Also, use of the L2 data could double the number of measurements, potentially decreasing the position estimation error standard deviation by $\sqrt{2}$.

For Fig. 4a, based on the histogram and mean, the multiband antenna performed best, while the sharkfin performed worst. Based on the standard deviation, the patch antenna performed best, while the sharkfin performed worst.

For Fig. 4b, based on the histogram and mean, the multiband antenna performed best, while the sharkfin performed worst. Based on the standard deviation, the sharkfin performed worst, while the multiband antenna performed slightly better in the front and middle locations and the patch antenna worked best in the rear location.

The analyses above do not provide decisive results about which location yielded the best positioning results.

B. Multipath Analysis Results

This section analyzes L1 multipath through the estimate $z_1^s(k)$ as defined in eqn. (13). For each satellite, Table II displays the standard deviation (σ), the maximum value (Max), and the number of samples (N) used to compute the statistics after applying the elevation and signal strength masks. The mean of $z_1^s(k)$ is always zero, so is not included. The subtables are displayed with colored text corresponding to the day of the data collection: teal for Day 1, black for day 2, blue for day 3. The bar graphs in Fig. 5 presents the same standard deviation data in a different format.

Suspicious values (those larger than 3.5 meters) have been italicized. These values are suspicious because the multipath is expected to typically have magnitude less than three meters. These large values could be caused by the hardware (i.e., antenna and receiver) or the processing method (e.g., undetected cycle slips). The processing method is identical for all data; however, each antenna-receiver pair provides different data to the algorithms for processing. The number of suspicious values is affected by the choice of elevation and signal strength masks.

(a) Position estimation results from point-wise LS estimation.
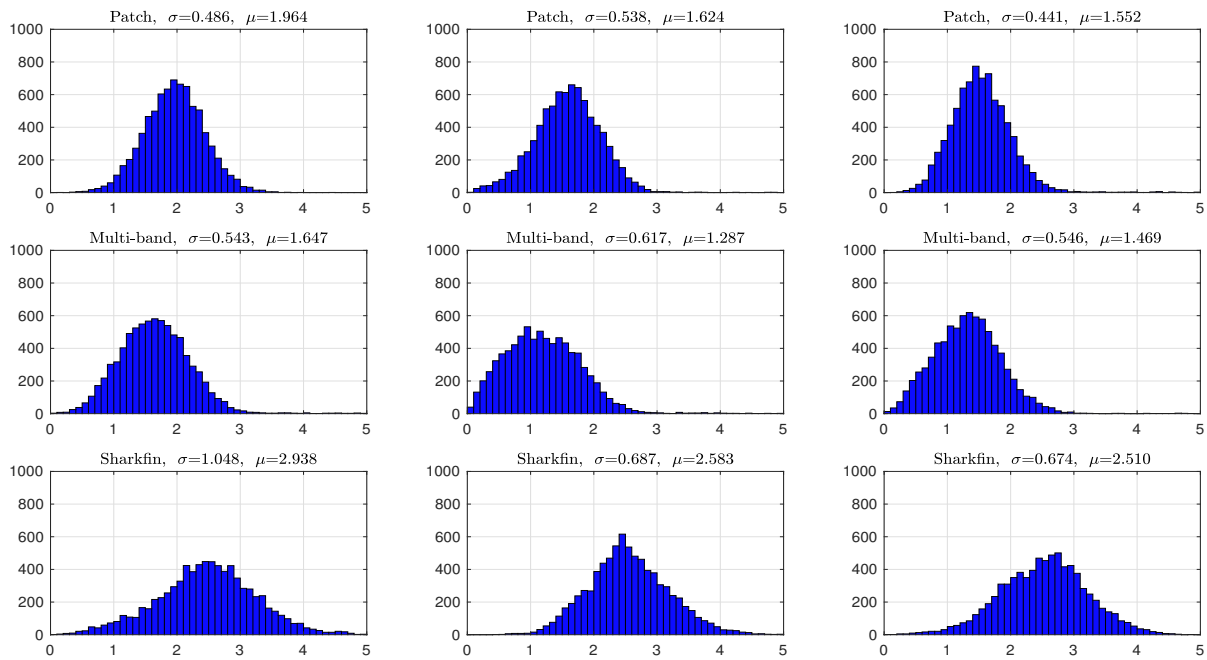
(b) Position estimation results from RTKLIB Extended Kalman Filter
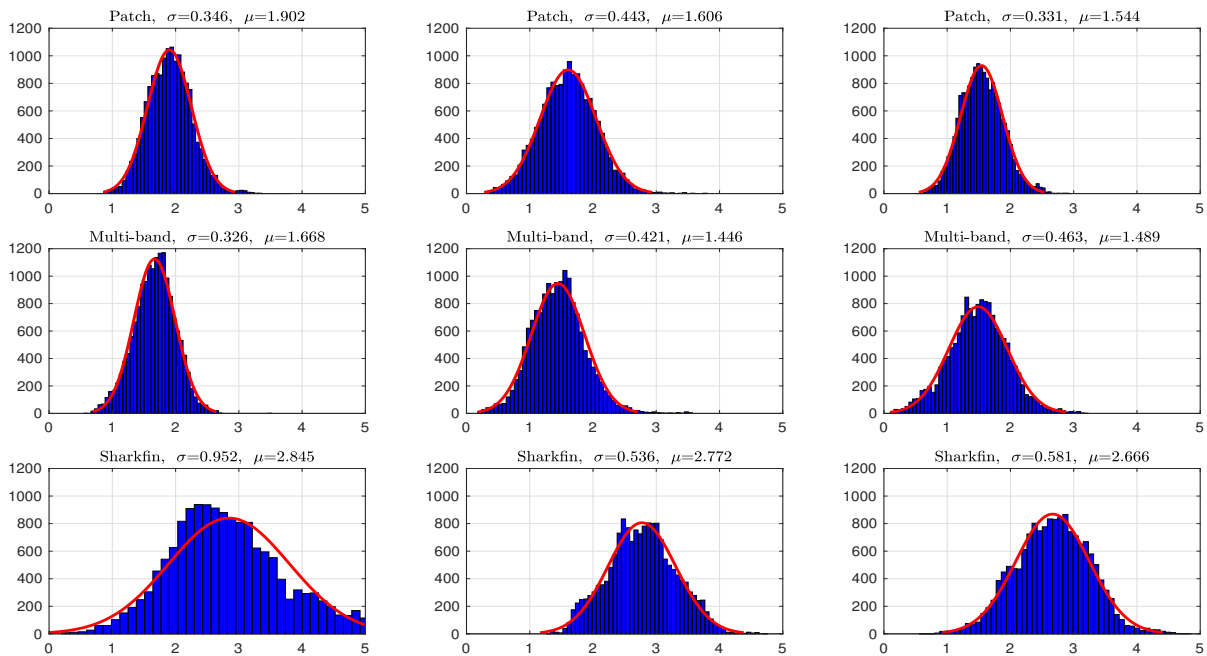

Figure 4: Histogram plots of the horizontal position error for each antenna at each location on the vehicle. The columns correspond to the three antenna positions: front on the left; middle in column 2; rear to the right. The rows correspond to the antennas (as labeled).

Table II Multipath Statistics per satellite for each antenna and location

		Front				Middle				Rear		
	PRN	**σ**	**Max**	**N**	**PRN**	**σ**	**Max**	**N**	**PRN**	**σ**	**Max**	**N**
Patch	3	0.46	1.41	9823	3	0.54	3.38	10439	3	0.39	1.55	10194
	8	0.46	1.18	4758	8	0.74	2.59	6332	8	0.28	1.21	6579
	9	0.39	1.17	12645	9	0.40	1.50	14399	9	0.41	1.75	14399
	14	0.27	0.93	1120	14	0.33	0.99	1311	14	0.32	0.91	1073
	16	0.98	6.48	10568	16	0.55	2.00	11551	16	0.26	0.99	11306
	22	0.39	1.26	7856	22	0.62	3.19	7980	22	0.23	1.13	7793
	23	0.34	1.21	12645	23	0.41	1.41	14399	23	0.33	1.21	14399
	26	0.29	1.19	7513	26	0.47	2.29	7698	26	0.35	1.11	7455
	27	0.59	3.27	6030	27	0.81	2.44	7600	27	0.27	1.10	7846
	30	0.43	1.34	4412	30	0.56	1.85	5977	30	0.63	1.97	6215
	31	0.33	0.98	1811	31	0.43	1.14	1998	31	0.34	1.15	1758
	PRN	**σ**	**Max**	**N**	**PRN**	**σ**	**Max**	**N**	**PRN**	**σ**	**Max**	**N**
Multiband	3	0.28	1.05	10193	3	0.36	1.25	9823	3	0.50	1.81	10439
	8	0.37	1.26	6580	8	0.42	1.13	4759	8	0.55	1.90	6332
	9	0.41	1.74	14399	9	0.49	1.98	12645	9	0.57	2.18	14399
	14	0.28	0.85	1072	14	0.36	1.00	1119	14	0.27	0.91	1311
	16	0.47	1.75	11305	16	0.63	1.95	10569	16	0.62	2.25	11551
	22	0.33	0.97	7792	22	0.40	1.31	7855	22	0.33	1.18	8038
	23	0.33	1.05	14399	23	0.41	1.48	12645	23	0.49	1.61	14399
	26	0.41	1.35	7454	26	0.31	1.45	7512	26	0.45	1.56	7698
	27	2.15	9.87	7826	27	0.47	2.07	6024	27	0.59	1.75	7601
	30	0.73	2.27	6216	30	0.46	1.30	4413	30	0.40	1.58	5977
	31	0.47	1.20	1757	31	0.36	1.07	1810	31	0.32	0.97	1998
	PRN	**σ**	**Max**	**N**	**PRN**	**σ**	**Max**	**N**	**PRN**	**σ**	**Max**	**N**
Sharkfin	3	1.17	4.82	10440	3	1.22	2.70	10194	3	1.07	3.16	9823
	8	0.83	3.48	6331	8	0.97	2.22	6579	8	0.51	1.78	4758
	9	5.81	12.51	14399	9	1.03	3.01	14399	9	1.06	3.27	12645
	14	0.42	1.10	1312	14	0.50	1.33	1073	14	0.30	0.80	1120
	16	0.75	3.88	11552	16	1.09	2.56	11306	16	0.61	2.29	10569
	22	1.08	4.49	8039	22	1.03	3.83	7793	22	0.49	2.31	7856
	23	0.93	3.00	14399	23	0.95	3.37	14399	23	0.67	1.91	12645
	26	0.60	2.31	7699	26	0.97	2.32	7455	26	0.64	2.45	7513
	27	0.69	2.88	7600	27	0.64	1.94	7846	27	0.44	1.58	6030
	30	1.15	5.64	5975	30	1.30	3.33	6215	30	0.54	1.59	4412
	31	0.79	1.82	1999	31	0.30	1.02	1758	31	0.38	1.10	1811

Because Table II contains results per satellite, it is difficult to digest. Table III displays the summary results computed as

$$\sigma_{al} = \left[\left(\frac{1}{\sum_{s=1}^{11} N_s} \right) \sum_{s=1}^{11} N_s \sigma_s^2 \right]^{1/2} \quad (16)$$

where a and l are defined as in eqn. (15), and N_s is the number of samples for satellite s in the rightmost column of each of the nine tables.

Regarding mounting location, the rear location gives better performance in most cases, but the inconsistencies prevent conclusive remarks. Regarding antenna performance, the Sharkfin performance was least favorable. Its standard deviations and maximum values are always higher than the other antennas. The patch and multiband antennas have similar performances levels. As stated earlier, the fact that the multiband antenna actually provides more measurements, could yield better positioning performance, especially in standard (non-differential) applications where it could remove ionospheric delay errors.

APPENDIX

A. Ground Truth Determination

The NRCan CSRS-PPP service [12], [13] was used to determine the ground truth position for each antenna in its test
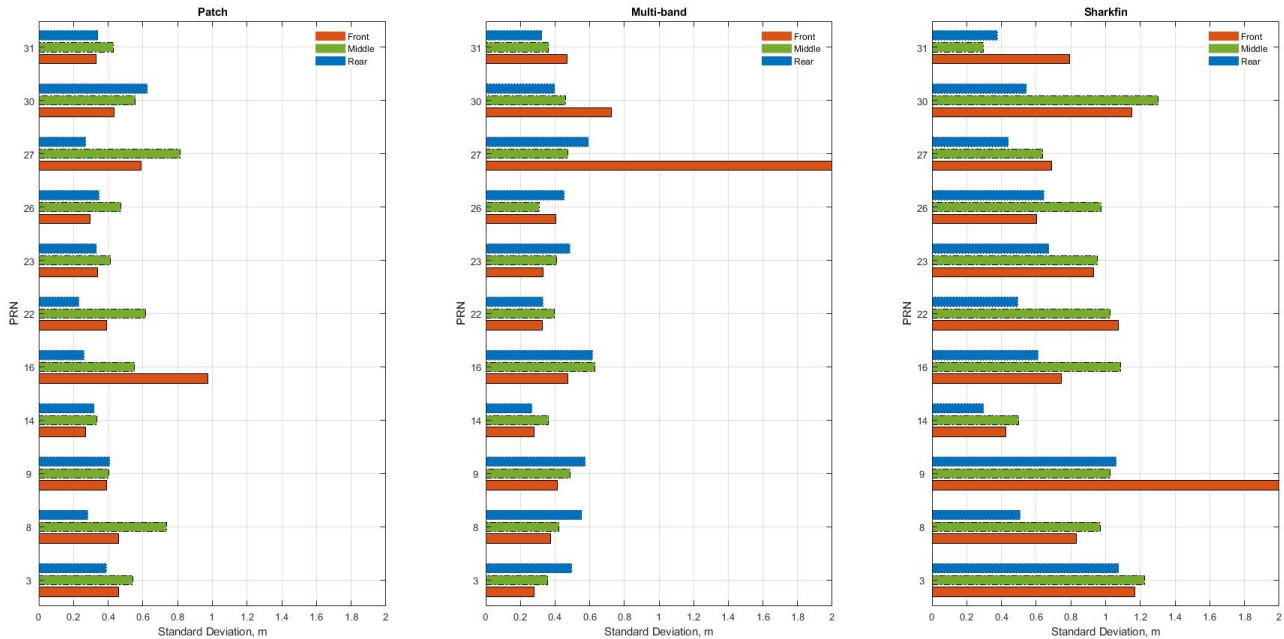
Figure 5: Multipath standard deviation.

locations in each experiment. This service is used by uploading the full set of raw pseudorange and phase measurements. The NRCan service uses its own Rapid clock and orbits products to achieve position estimation accuracy comparable to IGS Rapid products [14].

Table IV shows the results. Recall from Section II that the car was left parked in the same location, without movement, for the three day duration of the experiment. The first column denotes the antenna: (a) u-blox patch, (b) u-blox multi-band, and (c) MOPAR sharkfin. The second column indicates the antenna location on the vehicle. The third column shows the position relative to the point $(-2430906.000, -4702236.000, 3546651.000)$. This point was subtracted from the ground truth locations in Table V only for the convenience of presentation of the table. The positions are expressed in the IGS14 Earth-Centered-Earth-Fixed reference frame which is aligned to ITRF14 (version 2019.8).

Note the positioning accuracy disparity indicated by the standard deviation between the multi-band antenna (b) relative to the single frequency antennas (a) and (c). Estimated positions for Antenna (b) were computed using code and carrier-phase observations on two frequencies for both GPS and GLONASS

Table IV Summary of NRCan CSRS-PPP Position Estimates

Antenna	Location	Position, m	std, m
(a)	Front	$(-0.81, -0.60, 0.96)$	$(0.53, 0.29, 0.22)$
(b)	Front	$(-0.97, -0.61, 0.94)$	$(0.02, 0.02, 0.01)$
(c)	Front	$(-0.38, -0.60, 1.33)$	$(1.71, 0.86, 0.68)$
(a)	Middle	$(-1.54, -0.17, 1.05)$	$(1.03, 0.38, 0.31)$
(b)	Middle	$(-1.58, -0.32, 0.97)$	$(0.09, 0.04, 0.03)$
(c)	Middle	$(-1.43, -1.16, 1.36)$	$(0.83, 0.49, 0.38)$
(a)	Rear	$(-2.07, -0.02, 1.07)$	$(0.64, 0.37, 0.28)$
(b)	Rear	$(-1.93, -0.10, 0.96)$	$(0.02, 0.02, 0.01)$
(c)	Rear	$(-1.67, -0.90, 1.36)$	$(1.81, 0.65, 0.51)$

(L1C/L1CA and L2C). The estimated positions for the other two antennas only used single frequency data. Due to the increased accuracy of the multiband antenna, throughout the report, we use the NRCan CSRS-PPP position estimate of the multi-band antenna at each mounting location as the ground truth for that location. These locations are summarized in Table V.

As a cross-check, the distance between the marked antenna mounting locations on the masking tape were measured with a tape measure prior to data collection. The antenna separations from the tape-measure and from the NRCan estimated positions are shown in Table VI. The discrepancies are due to a combination of: estimate accuracy (as indicated in the right column), actual antenna placement relative to marked tape locations (error less than a centimeter), and measurements at different locations (along the tape for the tape measure or between antenna effective phase

Table III Summary of Multipath Statistics from Table II

	Front	Middle	Rear
Patch	0.52	0.55	0.36
Multiband	0.75	0.45	0.51
Sharkfin	2.47	1.02	0.75

Table V Summary of Ground Truth Position Information

Location	Position, m	std, m
Front	$(-0.97, -0.61, 0.94)$	$(0.02, 0.02, 0.01)$
Middle	$(-1.58, -0.32, 0.97)$	$(0.09, 0.04, 0.03)$
Rear	$(-1.93, -0.10, 0.96)$	$(0.02, 0.02, 0.01)$

Table VI Tape-measured and Estimated Antenna Separation

Locations	Measured, cm	Estimated, cm
Front-Middle	58.2	67.5 ± 13.1
Middle-Rear	47.5	41.3 ± 13.1
Rear-Front	105.6	108.7 ± 6.0

center locations for NRCan CSRS-PPP estimates).

B. The Ionospheric Estimate: $\hat{I}_{r,1}^s$

The method described in Section V removes an estimate of the Ionospheric delay in eqn. (11). This section discusses a methods to compute that Ionospheric delay estimate $\hat{I}_{r,1}^s$ using multi-frequency signal combinations [10], [11], [15].

When measurements on two carrier frequencies $j \in (L_1, L_2)$ are available, more detailed measurement models are useful:

$$\rho_{r,j}^s = R_r^s + c(dt_r - dt^s) + I_{r,j}^s + T_r^s + M_{p,j}^s$$
$$+ c(d_{r,j} - d_j^s + \delta t^{rel}) + \xi_{r,j}^s + \eta_{\rho_j}^s \tag{17}$$
$$\phi_{r,j}^s = R_r^s + c(dt_r - dt^s) - I_{r,j}^s + T_r^s + m_{\phi,j}^s + \lambda_j(\psi_r^s + N_{r,j}^s)$$
$$+ c(\delta_{r,j} - \delta_j^s + \delta t^{rel}) + \zeta_{r,j}^s + \eta_{\phi_j}^s \tag{18}$$

The symbols in these equations are defined in Table VII.

The difference of the phase between the two frequencies

$$x_2^s(k) = \phi_{r,1}^s(k) - \phi_{r,2}^s(k), \tag{19}$$

using eqn. (18), has the model (dropping time dependence to shorten the notation):

$$x_2^s = -I_{r,1}^s + m_{\phi,1}^s + \lambda_1 \psi_r^s + a_1^s + \eta_{\phi_1}^s$$
$$+ I_{r,2}^s - m_{\phi,2}^s - \lambda_2 \psi_r^s - a_2^s - \eta_{\phi_2}^s$$
$$= I_{r,2}^s - I_{r,1}^s + a_1^s - a_2^s$$
$$+ (\lambda_1 - \lambda_2)\psi_r^s + m_{\phi,1}^s - m_{\phi,2}^s + \eta_{\phi_1}^s - \eta_{\phi_2}^s$$

where all of the constant terms for each frequency are combined into the constants [16]:

$$a_1^s = \lambda_1 N_{r,1}^s + c(\delta_{r,1} - \delta_1^s) + \zeta_{r,1}^s$$
$$a_2^s = \lambda_2 N_{r,2}^s + c(\delta_{r,2} - \delta_2^s) + \zeta_{r,2}^s$$

The quantity $I_{r,2}^s - I_{r,1}^s$ is the portion of this equation that is of interest for computing $\hat{I}_{r,1}^s$; therefore, it is worth considering alone.

The L1 and L2 ionospheric delays are related to $I_{r,a}^s = \frac{40.3}{f_1 f_2} TEC$ by

$$I_{r,1}^s = \frac{f_2}{f_1} I_{r,a}^s \quad \text{and} \quad I_{r,2}^s = \frac{f_1}{f_2} I_{r,a}^s \tag{20}$$

Table VII Definition of symbols.

Symbol	Description
$d_{r,j}, d_j^s$	Receiver and satellite instrument delays (assumed constant)
$dt_r, dt^s, \delta t^{rel}$	Receiver, satellite, and relativistic clock error
$I_{r,j}^s$	Ionospheric delay at frequency j
$m_{\phi,j}^s$	phase multipath
$N_{r,j}^s$	Phase ambiguity (assumed constant)
R_r^s	Geometric range between the antenna phase centers of satellite s and receiver r
T_r^s	Tropospheric delay
$\eta_{\phi_j}^s$	Phase measurement noise at frequency j
$\eta_{\rho_j}^s$	Pseudorange measurement noise at frequency j
$\zeta_{r,j}^s$	Antenna phase-center offsets and variations (assumed constant)
$\delta_{r,j}, \delta_j^s$	Receiver and satellite instrument delays (assumed constant)
$\xi_{r,j}^s$	Group delay variations or code-phase patterns (assumed constant)
ψ_r^s	Antenna phase wind-up (in cycles)

where TEC is the total electron count along the signal path. The difference

$$I_{r,2}^s - I_{r,1}^s = \frac{f_1}{f_2} I_{r,a}^s - \frac{f_2}{f_1} I_{r,a}^s = \left(\frac{f_1^2 - f_2^2}{f_1 f_2} \right) I_{r,a}^s; \tag{21}$$

therefore,

$$x_2^s = \left(\frac{f_1^2 - f_2^2}{f_1 f_2} \right) I_{r,a}^s + (a_1^s - a_2^s) \tag{22}$$
$$+ (\lambda_1 - \lambda_2)\psi_r^s + (m_{\phi,1}^s - m_{\phi,2}^s) + (\eta_{\phi_1}^s - \eta_{\phi_2}^s)$$
$$= \left(\frac{f_1^2 - f_2^2}{f_1 f_2} \right) I_{r,a}^s + a_{1,2}^s + (\lambda_1 - \lambda_2)\psi_r^s + m_{\phi_{1,2}}^s + \eta_{\phi_{1,2}}^s \tag{23}$$

where $a_{1,2}^s = a_1^s - a_2^s$ is constant, $m_{\phi_{1,2}}^s = m_{\phi,1}^s - m_{\phi,2}^s$ is small, and $\eta_{\phi_{1,2}}^s = \eta_{\phi_1}^s - \eta_{\phi_2}^s$ is small. Define the new signal
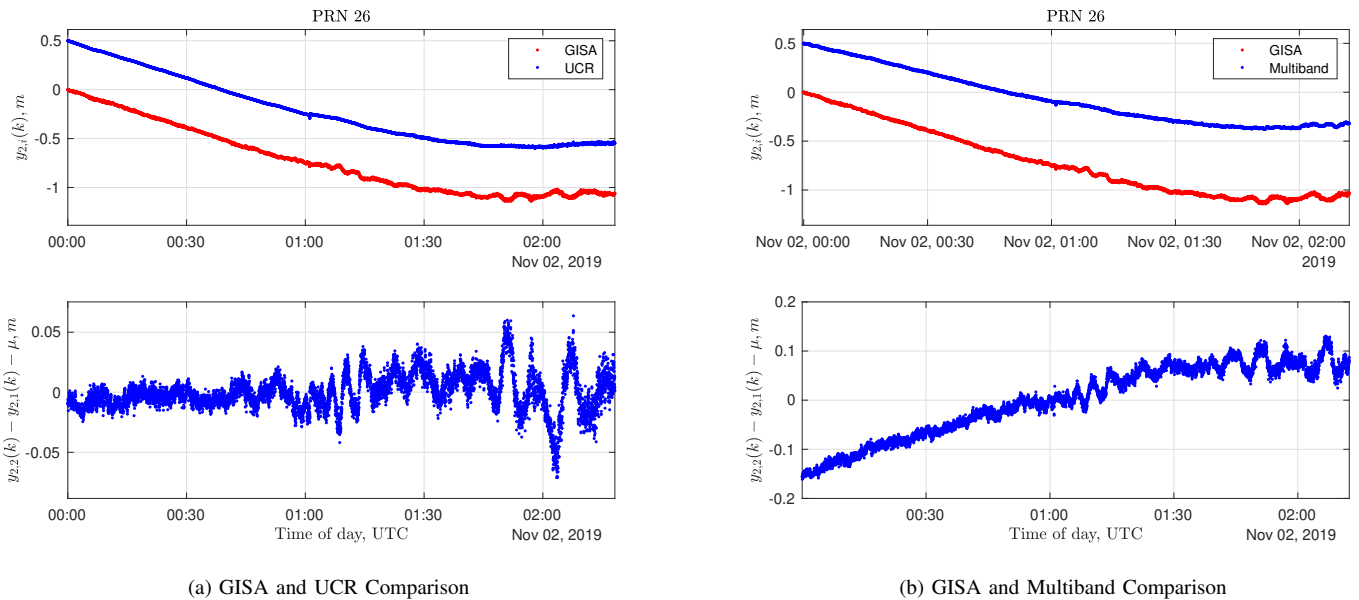
$$y_2^s(k) = \left(\frac{f_2^2}{f_1^2 - f_2^2} \right) x_2^s(k) \tag{24}$$

which has the model

$$y_2^s(k) = \left(\frac{f_2}{f_1} \right) I_{r,a}^s(k) + A\left(a_{1,2}^s + (\lambda_1 - \lambda_2)\psi_r^s + m_{\phi_{1,2}}^s + \eta_{\phi_{1,2}}^s \right)$$
$$= I_{r,1}^s(k) + A a_{1,2}^s \tag{25}$$
$$+ A\left((\lambda_1 - \lambda_2)\psi_r^s(k) + m_{\phi_{1,2}}^s(k) + \eta_{\phi_{1,2}}^s(k) \right)$$

where $A = \left(\frac{f_2^2}{f_1^2 - f_2^2} \right)$.

Eqn. (25) shows that the signal $y_2^s(k)$ is the desired signal $I_{r,1}^s(k)$ plus a constant $A a_{1,2}^s$, and the small time-varying term. The time-varying term (in the second line) includes receiver

(a) GISA and UCR Comparison

(b) GISA and Multiband Comparison

Figure 6: Comparison of ionospheric delay estimates for PRN 26. The curves in the top row show the ionospheric estimate from two different antenna-receiver pairs. The bottom row corresponds shows the difference of the two curves with the corresponding mean (constant bias) subtracted.

noise $\eta^s_{\phi_{1,2}}$ (millimeter-level), multipath $m^s_{\phi_{1,2}}$ (centimeter-level), and receiver-satellite relative rotation effects described as phase wind-up (see pages 85-87 and 569-572 in [17]). The phase wind-up denoted by ψ^s_r is due to the GPS signals being circularly polarized. Twice per orbit each satellite vehicle rotates 180 degrees (i.e., half a cycle). Because $(\lambda_1 - \lambda_2)$ has a magnitude of 0.054 m and $A = 1.55$, each half cycle of satellite rotation causes 0.04 m of change in y^s_2. The satellite rotation rate is less than 0.2 deg/s (0.0006 cycles/sec), so this maneuver requires about 900 seconds. The rate of change of y^s_2 due to the satellite portion of phase wind-up changes at less than 50×10^{-6} m/s ($0.0006A(\lambda_1 - \lambda_2)$). These effects are considered negligible for the analysis herein.

When $y^s_2(k)$ is used in eqn. (11) in place of $\hat{I}^s_{r,1}(k)$, then Step 3 will remove the constant. The small time variations have maximum magnitude of centimeters and will be neglected.

All experimental results in this report use the GISA CORS station GPS data to compute the ionospheric estimate for all antennas.

C. Example of Estimating $I^s_{r,a}$

This section presents examples of estimating the L1 ionospheric delay using the method described in Appendix B.

Fig. 6 contains results for PRN 26. The top two subfigures contain two curves. The left figure compares the ionospheric estimates from two survey quality two-frequency antennas and receivers: UCR[1] and GISA. The right figure compares the ionospheric estimates of the GISA and u-blox multiband antenna and receiver. Due to the superior antenna hardware design [18], [19]

[1]This UCR base station uses a Novatel OEMV-2 receiver with an L1/L2 antenna.

and clever receiver correlation techniques [20]–[22] of the more expensive equipment, the GISA and UCR base stations should be better able to mitigate phase multipath than the less expensive antennas and receivers that are the focus of this study.

Because the next step in the multipath estimation process removes the mean of the signal, the shape of the graph is the critical point of comparison. To facilitate the comparison of the shapes of the curves, in the top figure the curves have been shifted vertically by adding a constant selected to make the curves near each other along the vertical scale.

In comparing the multiband estimate with the GISA and UCR estimates it is important to recall that the estimates from the GISA and UCR base stations are obtained using the precise legacy L2P signals whereas the multiband antenna-receiver use L2C.

The important points to note relative to the red and blue curves in both top figures are: (1) They have the same shape; (2) They are offset with respect to each other by a (relatively) constant amount. Both plots follow the same trend despite having different y-intercepts, due to constant biases, as discussed relative to Eqn. (25). Therefore, the error in the multipath estimate due to removal of the ionospheric estimate is expected to be small and very slowly time varying in comparison to code multipath.

D. Elevation and Signal Strength Thresholds

The utility of satellite signals for position estimation depends critically on the signal quality. It is well know that signal quality deteriorates with decreasing satellite elevation and signal strength. For the results herein, we only used satellite data when the elevation was greater than 15 degrees and the signal strength was larger that 30 dB.
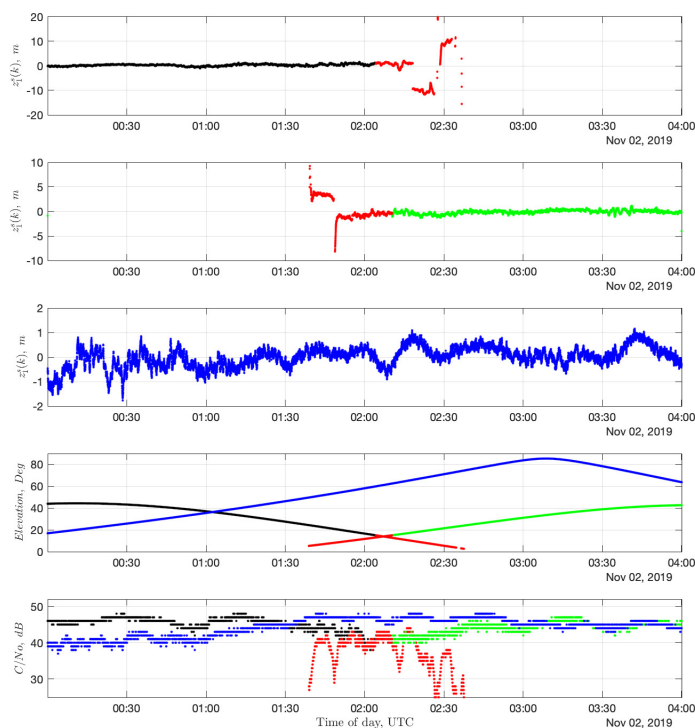
Figure 7: Estimated multipath signal $z_1^s(k)$ for *PRN* 26, 8, and 9 (first, second, and third rows, respectively) in the same location on the vehicle. The fourth and bottom rows are satellite elevation and carrier-to-noise ratio of L1.

Fig. 7 shows the estimated multipath signal for three different satellites. All signals that are used for a given satellite are in the same color: black for SV 26; green for SV 8; and, blue for SV 9. All signals in this figure are measured using the multiband antenna. The elevation and signal strength of each satellite is shown in the bottom two figures. The portion of each graph that is displayed as red represents those samples that were discarded due to either the elevation or signal strength masks.

Even at low elevations, the signal-strength was often above its threshold. Therefore, most of the discarded samples were due to the elevation mask. The top two subfigures of Fig. 7 show that the stated selection criteria successfully remove satellites prior to signal misbehavior.

E. Acknowledgment

REFERENCES

[1] Anonymous, "ZED-F9P: u-blox F9 high precision GNSS module," u-blox, Tech. Rep., 2019. [Online]. Available: https://www.u-blox.com/en/product/zed-f9p-module

[2] D. A. Braasch, Y. Liu, and D. R. Corey, "Multipath effects," in *Global Positioning System: Theory and Applications*, 1996.

[3] J. A. Farrell, *"Aided Navigation: GNSS with High Rate Sensors"*. McGraw-Hill Inc, 2008.

[4] B. Hofmann-Wellenhof, H. Lichtenegger, and J. Collins, *"Global Positioning System: Theory and Practice"*. Springer Science & Business Media, 2012.

[5] M. S. Braasch, "Multipath," in *Handbook of Global Navigation Satellite Systems*, P. J. G. Teunissen and O. Montenbruck, Eds. Springer International Publishing, 2017, pp. 443–468.

[6] A. Hauschild, "Basic Observation Equations," in *Handbook of Global Navigation Satellite Systems*, P. J. G. Teunissen and O. Montenbruck, Eds. Springer International Publishing, 2017, pp. 561–582.

[7] ——, "Combinations of Observations," in *Handbook of Global Navigation Satellite Systems*, P. J. G. Teunissen and O. Montenbruck, Eds. Springer International Publishing, 2017, pp. 583–604.

[8] P. D. Groves, Z. Jiang, M. Rudi, and P. Strode, "A portfolio approach to NLOS and multipath mitigation in dense urban areas," *Navigation*, 2013.

[9] T. Takasu, "RTKLIB: An open source program package for GNSS positioning," *Tech. Rep., 2013.*, 2011.

[10] R. Hatch, "The synergism of GPS code and carrier measurements," in *Int. Geod. Symp. on Sat. Dopp. Pos.*, 1983, pp. 1213–1231.

[11] R. Hatch, J. Jung, P. Enge, and B. Pervan, "Civilian GPS: The benefits of three frequencies," *GPS Solutions*, vol. 3, no. 4, pp. 1–9, 2000.

[12] P. Tétreault, J. Kouba, P. Héroux, and P. Legree, "CSRS-PPP: an Internet service for GPS user access to the Canadian Spatial reference frame," *Geomatica*, vol. 59, no. 1, pp. 17–28, 2005.

[13] F. Lahaye, Y. Mireault, P. Héroux, P. Tétreault, and J. Kouba, "Online precise point positioning: A new, timely service from natural resources canada," *GPS World*, 2008.

[14] G. Cerretto, P. Tavella, F. Lahaye, Y. Mireault, and D. Rovera, "PPP using NRCan ultra rapid products (EMU): Near real-time comparison and monitoring of time scales generated in time and frequency laboratories," in *Int. Conf. IEEE Int. Freq. Control and the Eur. Freq. and Time Forum (FCS)*, 2011, pp. 1–6.

[15] R. Hatch, "Instantaneous ambiguity resolution," in *Kinematic Systems in Geodesy, Surveying, and Remote Sensing*. Springer, 1991, pp. 299–308.

[16] R. Warnant, "Reliability of the TEC Computed Using GPS Measurements — The Problem of Hardware Biases," *Acta Geodaetica et Geophysica Hungarica*, vol. 32, no. 3, pp. 451–459, 1997.

[17] P. Teunissen and O. Montenbruck, *Handbook of Global Navigation Satellite Systems*. Springer International Publishing, 2017.

[18] P. C. Fenton and J. Jones, "The theory and performance of novatel inc.'s vision correlator," in *Proc. ION GNSS*. Citeseer, 2005, pp. 2178–2186.

[19] F. Bletzacker, "Reduction of multipath contamination in a geodetic GPS receiver," in *Proc. 1st Int. Symp. Precise Position. Glob. Position. Syst.* US Department of Commerce, National Oceanic and Atmospheric Administration, 1997, pp. 413–422.

[20] L. R. Weill, "GPS multipath mitigation by means of correlator reference waveform design," in *Proceedings of the National Technical Meeting, Institute of Navigation*, 1997.

[21] M. Paonni, J.-A. Avila-Rodriguez, T. Pany, G. W. Hein, and B. Eissfeller, "Looking for an optimum s-curve shaping of the different mboc implementations," *ION Navigation*, vol. 55, no. 4, pp. 255–266, 2008.

[22] L. R. Weill, "Application of superresolution concepts to the GPS multipath mitigation problem," in *Proc. ION NTM 1998, Long Beach (ION, Virginia 1998)*, 1998, pp. 673–682.